ACS APPLIED MATERIALS & INTERFACES

Research Article

www.acsami.org

Microfluidic Foaming: A Powerful Tool for Tailoring the Morphological and Permeability Properties of *Sponge-like* Biopolymeric Scaffolds

Marco Costantini,[†] Cristina Colosi,[†] Jakub Jaroszewicz,[‡] Alessia Tosato,[†] Wojciech Święszkowski,[‡] Mariella Dentini,[†] Piotr Garstecki,[§] and Andrea Barbetta*[,†]

[†]Department of Chemistry, Sapienza University of Rome, 00185 Rome, Italy

[‡]Faculty of Materials Science and Engineering, Warsaw University of Technology, 02507 Warsaw, Poland

[§]Institute of Physical Chemistry, Polish Academy of Sciences, 01224 Warsaw, Poland

Supporting Information

ABSTRACT: Ordered porous polymeric materials can be engineered to present highly ordered pore arrays and uniform and tunable pore size. These features prompted a number of applications in tissue engineering, generation of meta materials, and separation and purification of biomolecules and cells. Designing new and efficient vistas for the generation of ordered porous materials is an active area of research. Here we investigate the potential of microfluidic foaming within a flow-focusing (FF) geometry in producing 3D regular *sponge-like* polymeric matrices with tailored morphological and permeability properties. The challenge in using microfluidic systems for the generation of polymeric foams is in the high viscosity of the continuous phase. We demonstrate that as the viscosity of the aqueous solution increases, the accessible range of foam bubble fraction (Φ_b) and bubble diameter (D_b) inside the microfluidic chip tend to narrow progressively. This effect limits the accessible range of geometric properties of the resulting materials. We further show that this problem can be rationally tackled by appropriate choice of the concentration of the polymer. We demonstrate that via such optimization, the microfluidic assisted synthesis of porous materials becomes a facile and versatile tool for generation of porous materials with a wide range of pore size and pore volume. Moreover, we demonstrate that the size of interconnects among pores—for a given value of the gas fraction—can be tailored through the variation of surfactant concentration. This, in turn, affects the permeability of the materials, a factor of key importance in flow-through applications and in tissue engineering.

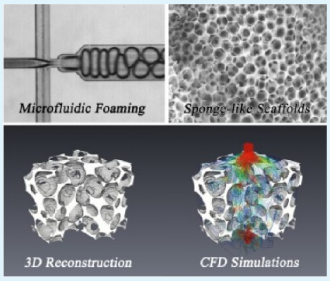

KEYWORDS: *microfluidic foaming, scaffolds, ordered porous structure, alginate, solution viscosity, microcomputed X-ray tomography*

1. INTRODUCTION

Hydrogels derived from natural polymers are frequently the materials of choice in biomedical applications such as drug delivery carriers and tissue engineering (TE) scaffolds due to their hydrophilic nature and physical properties that resemble those of the native extracellular matrix. Thanks to these characteristics, they can be implanted in the human body, eliciting only minimal adverse effects. In TE, hydrogels can be employed as cell embedding media or as porous scaffolding materials. In the former application, cells are suspended in the hydrogel precursors and can be directly delivered to the specific site in a minimally invasive way, for example, using laparoscopic devices.[1−3] An external stimulus (light, temperature) is contextually applied to induce gelation of the solution. This process permits spatial and temporal control over the conversion of a liquid to a gel, so that complex shapes can be obtained. In the latter application, a porous matrix is first fabricated and then seeded with cells in either a static or dynamic environment. The formation of a porous structure constitutes a central goal of scaffold fabrication, and a number of techniques were developed to achieve this goal including phase separation,[4−6] solvent casting/particulate leaching,[7−10] gas foaming,[11−15] emulsion templating,[16−19] and freeze-drying.[20−24] Because of the relative ease in using these techniques to fabricate scaffolds, they are still commonly used. A core limitation of these technologies is the lack of precise control over scaffold specifications such as pore size, shape, distribution, and interconnectivity as well as the overall scaffold shape. Inhomogeneity in porous texture has caused scaffolds to be much less successful than their potential suggests. Previous study reveals that if the pore size has high variability, this will create impediments to cell seeding and growing.[25] To decrease the effect of the structure, highly ordered and uniform spatial structures are preferable. A uniform porous texture guarantees a more homogeneous distribution of cells and an even mass transfer in all compartments of the scaffold.[26−29]

Received: August 6, 2015
Accepted: October 5, 2015
Published: October 5, 2015

DOI: 10.1021/acsami.5b08221
ACS Appl. Mater. Interfaces 2015, 7, 23660−23671

In response to these issues, Ratner et al. used templating poly(methyl methacrylate) (PMMA) microspheres to create monodisperse and interconnected porous hydrogel scaffolds.[30] This was done through packing monodisperse PMMA microspheres in a microchannel, and the microspheres were partially sintered to create interconnects. A UV polymerizable hydrogel was then flowed through sphere interstices and polymerized using a UV lamp to cure the continuous phase. The PMMA microspheres were then dissolved out using acetone, leaving the hydrogel scaffold with interconnected pores. Analogously, Ma et al. used monodisperse paraffin beads as the porogenic phase to create gelatin scaffolds characterized by well-defined pore and interconnect sizes.[31] This method, known as inverse opal templating, worked well to fabricate porous hydrogel scaffolds, but the use of a toxic solvent to dissolve the templating microspheres makes the derived scaffold undesirable for biological applications. Furthermore, the range of solid fraction is limited due to the condition of colloidal crystal assembly, and the pore size depends on the availability of colloidal microspheres. In addition, the method is quite labor intensive because it involves the synthesis of the porogenic particles by conventional emulsion polymerization technique and their fractionation according to their dimension and is limited to the fabrication of scaffolds small in size.

In such a scenario, microfluidics foam templating may represent a valid alternative for the synthesis of tailored porous hydrogels.[32,33] Microfluidics, which manipulates fluidic flow on microscales, provides new means to generate monodisperse bubbles or droplets at the length scale of 100 μm. The use of an inert gas as the dispersed phase guarantees biocompatible synthetic conditions. Not only are pores of the ensuing materials highly monodipersed in size and can be tuned within a wide range, but also the eventual presence, number, and size of communicating windows among pores (hereinafter indicated as interconnects) can be controlled, as well as the spatial pore order along medium- to long-scale distances. An additional important factor that generates interest in microfluidics foam/emulsion templating stems from the flexibility in choosing the polymer chemistry to adapt the materials to various applications. To take full advantage of this flexibility, the methods of generation of the porous structure should preferably be independent of the specific chemical character of the polymer in the drive to decouple the process of generation of the geometric structure of the material from its chemical properties.

Polymers so far employed within microfluidic emulsion/foam templating consisted of low molecular weight poly(vinyl alcohol),[32] dextran,[33] gelatin,[34] and polyacrylamide.[35,36] These polymers enjoy a high degree of chain flexibility and, as a consequence, the viscosities of the corresponding concentrated solutions do not represent a major issue in the context of microfluidic assisted synthesis of porous materials. On the other hand, in tissue engineering practice, biopolymers characterized by a relatively stiff backbone are often used as scaffolding materials due to their benign biological properties.[37−39] Biopolymers such as hyaluronic acid, alginate, chondroitin sulfate, and chitosan impart to solutions relatively high viscosities even at low concentrations. Because broadening the potentials of microfluidics emulsion/foam templating in the synthesis of scaffolds for TE through the employment of the above-mentioned biopolymers is of practical interest, in the present work we intend to shed some light on the role of solution viscosity in conditioning the porous structure of the derived porous matrices. As a model biopolymer we use alginate, a polysaccharide with a relatively stiff backbone that enjoys a vast popularity in material science and in the biomedical area.[40,41] Furthermore, alginate is inexpensive, and a range of different molecular weights are commercially available. Microfluidics alginate porous matrices were first synthesized by Martynov et al. using a device constituted by two capillary tubes connected in a T-junction mode. The obtained materials were characterized by random morphologies as witnessed by broad pore size distributions and the absence of any space correlation among pores.[42]

In this work we performed for the first time a systematic investigation correlating polymer solution viscosity and foam pattern inside a microfluidic system. This correlation is crucial for the successful synthesis of materials with tunable porous properties. The paper is organized as follows: first, we establish calibration diagrams regarding the accessible ranges of bubble size and gas volume fraction as a function of solution flow rates and viscosity; second, we report on the porous and permeability characteristics of the materials obtained; finally, we provide some data on foam production rate and stress how the limited rate of foam production in conjunction with foam stability is one of the major problem encountered in the fabrication of porous materials via microfluidic foaming.

2. MATERIALS AND METHODS

2.1. Materials. Alginate (ALG) was a kind gift of FMC (Italy) and is characterized by an average molecular weight (M_w) of 33 kg/mol and a polydispersity index of 1.4 as determined by gel permeation chromatography (GPC). *N*-Ethyl-*N*′-[3-(dimethylamino)propyl]-carbodiimide hydrochloride (EDC) *N*-hydroxysuccinimide (NHS), 2-[*N*-morpholino]ethanesulfonic acid buffer (MES), cetyltrimethylammonium bromide (CTABr), and $CaCl_2$ were purchased from Sigma-Aldrich and used without further purification. Alginate was purified by precipitation in acetone from a ≈1% w/v aqueous solution. The precipitate was dissolved again in water and put into 2000 molecular weight cutoff dialysis tubes. Dialysis water was changed regularly three times a day until it reached the conductivity of distilled water (2 μS/cm). The pH of the solution was adjusted to 7.0, and then it was filtered through 0.45 μm cellulose acetate filters and finally freeze-dried.

The continuous phase of the foams consisted of a solution of alginate (ALG) and CTABr at various concentrations. As the dispersed gaseous phase, filtered air was used.

2.2. Production of Polycarbonate Chip. The chip used in all of the experiments was realized with a CNC milling machine (MSG402, ErgWind, Poland) on a polycarbonate (PC) sheet 5 mm in thickness. After milling, the device was sonicated in isopropanol for 30 min and then sealed with a hot press at 130 °C for about 30 min. After this period of time, the sealed chip was allowed to cool slowly to room temperature. In Figure 1a the characteristic dimensions of the channels within the chip are shown.

2.3. Microfluidic Foaming. The mechanism of production of monodisperse bubbles within FF devices has been largely investigated. Briefly, the gaseous and liquid phases meet orthogonally upstream of a tight junction. The gaseous phase periodically penetrates inside the orifice, inflates a bubble, and then is squeezed by the liquid phase (Figure 1b).

In microfluidic foaming experiments, we used as the continuous phase three different aqueous solutions with an alginate content of 5, 10, and 15% w/w and the same concentration of CTABr of 5% w/w. To study the effect of the surfactant concentration on the process of interconnect opening, we fixed the concentration of alginate to 5% w/w and varied the concentration of CTABr: 0.6, 1.0, and 5.0% w/w.

As will be shown, the flow focusing geometry allows for the production of customized foams. The parameters that were changed during experiments were the applied gas pressure (P_g) and the liquid

DOI: 10.1021/acsami.5b08221
ACS Appl. Mater. Interfaces 2015, 7, 23660−23671

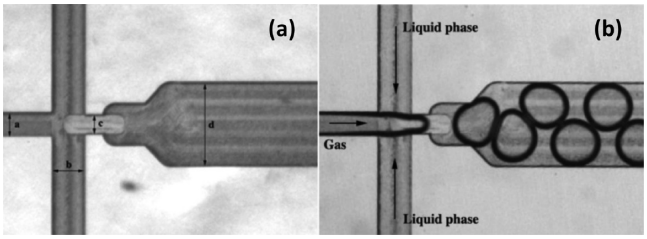

Figure 1. (a) Light micrograph of the microfluidic chip engraved on PC sheet. Characteristic dimensions of the chip: gas inlet = 200 μm; liquid phase inlet = 300 μm; orifice width (w_{or}) = 150 μm; outlet channel width (w_{out}) = 700 μm. The depth of the channels (h) is 150 μm. (b) At the right is shown the chip during the production of monodisperse bubbles.

flow rate (Q_l). Increasing P_g leads to a corresponding increment in bubble diameter, whereas an increase in Q_l implies a decrease in bubble diameter. The repeatability of the process lies in the fine-tuning of these two variables. For these reasons, the liquid phase was injected inside the chip through a microfluidic pump (neMESYS low pressure, Cetoni GmbH apparatus), whereas the gas flow was regulated with a precise pressure regulator (Rexroth, model 7290).

Equilibrium interfacial tension values are obtained using a du Nouy ring tensiometer (mgw-lambda Tensiometer, Lauda), and the measured values for each alginate + surfactant solution/air pair are given in Table 1. Rheological measurements of alginate solution

Table 1. Average Viscosity (η), Interfacial Tension (σ), and Capillary Number (Ca) of the Liquid Flow in the Orifice of the Microfluidic Chip for Solutions Characterized by Different Alginate Concentrations[a]

alginate solution (% w/w)	η (mPa·s)	σ (mN/m)	Ca
5	46	35.6	10^{-4}–10^{-3}
10	273	39.8	10^{-3}–10^{-2}
15	1100	44.6	10^{-2}–10^{-1}

[a]CTABr = 5% w/w.

viscosities as a function of shear rate were performed at 25 °C with a controlled stress rheometer (Bohlin CS10, version 4.033) with a coaxial cylinder geometry (C10).

2.4. Image Analysis. The production of the foams in the outlet channel was monitored continuously with a stereomicroscope (Nikon, SMZ1000) equipped with a Photron Fastcam 1024 PCI at 500 fps. The recorded videos were used to estimate the gaseous volume fraction (Φ_b) and the diameter of bubbles (D_b) of the produced foams. Φ_b was approximated to the ratio A_b/A, where A_b is the apparent area occupied by the gas in a section of a total area A. D_b was simply calculated from the volume of bubble $V_b = A_b h$, where h is the depth of the chip (150 μm).[43] All of the images and videos were processed with ImageJ software.

2.5. Scaffold Production. The experimental procedure followed consisted of regulating P_g and Q_l until a stable and close-packed 2D bubble pattern in the outlet channel was obtained. All of the scaffolds were produced with a dispersed phase fraction between 60 and 80%. When an acceptable amount of foam (≈1.5 mL) was collected inside a 3 mL glass vial, it was frozen in liquid nitrogen, to prevent the occurrence of instability phenomena, and then lyophilized. This was followed by the cross-linking step in which the structure of the scaffold is irreversibly locked in.

2.6. Cross-Linking Reaction and Purification of Scaffolds. The freeze-dried alginate scaffolds were physically cross-linked by soaking them in a solution 1 M $CaCl_2$ for 24 h. Then, the auto-cross-linking reaction between alginate hydroxyls and carboxylate groups was accomplished by means of the EDC/NHS system in 0.2 M MES buffer (pH 4.5). The molar ratio EDC:ALG (repeating units) was 1:3, whereas EDC:NHS was 1:5. The reaction was performed at room temperature for 48 h. Afterward, the samples were dialyzed extensively against ultrapure water until reaching the nominal conductivity of distilled water. Finally, the samples were freeze-dried again for characterization analysis.

2.7. Scanning Electron Microscopy (SEM). The structures of the scaffolds were investigated using SEM (Nova NanoSEM) operating at 5 kV. Prior to observation, fractured samples were mounted on aluminum stubs using adhesive carbon tape to increase the conductivity. All samples were observed without any sputtering.

2.8. Microcomputed Tomography (μCT) Analysis. μCT is a nondestructive technique that generates a stack of 2D cross-sectional images of a sample using an X-ray source. Through the manipulation of these 2D images, it is possible to create a 3D reconstruction of the sample and, as a consequence, to perform 3D analyses. Acquisition was performed on freeze-dried scaffolds using an Xradia MicroXCT-400 with the following parameters: 40 kV voltage, 10 W power, no filter material, and a 0.18 rotation step in an angle interval of 184°. The voxel size was the same for all of the samples (2.23 × 2.23 × 2.23 μm). Scanning was performed at atmospheric pressure and room temperature (25 °C). Reconstruction was performed using a standard filtered back-projection algorithm. Image analysis of data obtained from μCT was carried out following the same procedure described in a preceding work.[16]

2.9. Permeability Model. The permeability (k) of all scaffolds produced was calculated from μCT data using a commercial software suite (Avizo Fire with XLabHydro extension, FEI Visualization Science Group, Burlington, MA, USA). In all cases, simulations were performed over a 1 mm × 1 mm × 1 mm cubic volume of interest (VOI) that was considered as a representative volume of all samples.

To numerically estimate permeability, Avizo software solves the Navier–Stokes equations by a finite volume method and applies Darcy's law. The software performs the simulations of a permeability experiment by hermetically closing a given sample with four faces while virtual setups (i.e., additional shapes simulating the connection of the VOI under analysis with a perfusion system) are added on two opposite faces to guide the flow along one direction.

The solver works under the hypothesis of a Newtonian, incompressible fluid, under steady state laminar and no-slipping boundary conditions at solid/fluid boundaries.

For simulations, we set the value of pressure at the inlet to 1.5 bar, whereas the output pressure was set to atmospheric level (1 bar). The viscosity of the fluid was set to 1 cP.

3.0. RESULTS AND DISCUSSION

3.1. Foam Calibration Diagrams. Microfluidic systems are well-known as a tool for producing, handling, and processing monodisperse bubbles or droplets.[44] A very interesting and promising application in material science is represented by the use of this collection of monodisperse bubbles or droplets (produced generally within flow-focusing or T-junction chips) as templating systems for the production of highly ordered porous materials.

A rational approach to the design of the porous characteristics of materials produced via microfluidics consists of the determination of the calibration diagrams describing the accessible ranges for the gaseous volume fraction (Φ_b) and the bubbles diameter (D_b) within the designed chip upon variation of (i) the flow rate (Q_l), (ii) the viscosity of the liquid phase, and (iii) the gas pressure (P_g) of the dispersed phase.

Three different aqueous solutions with a content of alginate of 5, 10, and 15% w/w, respectively, and a constant concentration of CTABr (5% w/w) were prepared. The first two solutions, 5 and 10% w/w, exhibited a Newtonian behavior in the whole range of shear rate, from 10^0 to 10^3 s^{-1}, explored (Figure S1). The solution with the highest concentration (15% w/w) revealed a slightly shear-thinning behavior typical of systems that exhibit chains' association of either topological

DOI: 10.1021/acsami.5b08221
ACS Appl. Mater. Interfaces 2015, 7, 23660–23671

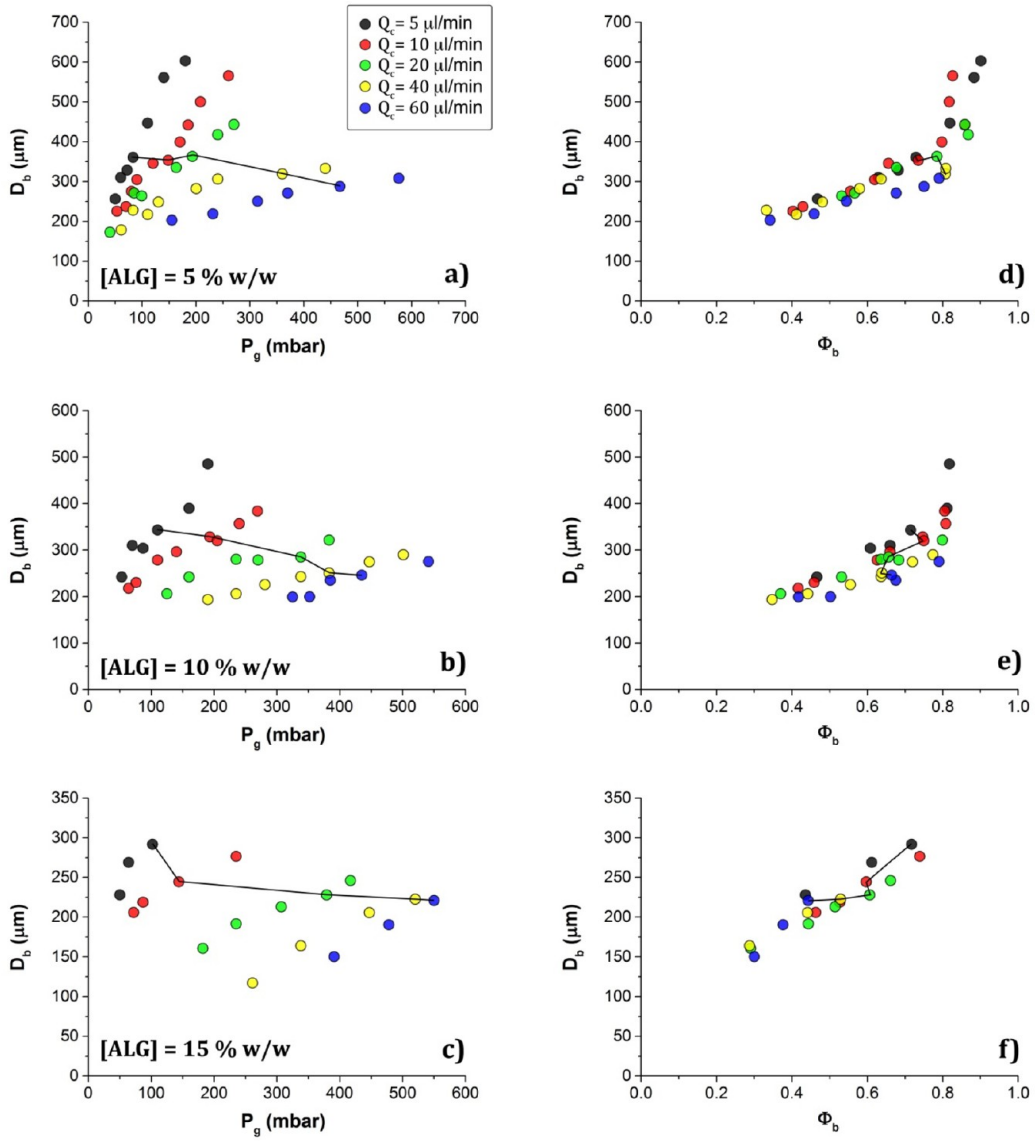

Figure 2. Accessible ranges of bubble diameter, D_b, as a function of either gas pressure, P_g, and flow rate of the aqueous phase, Q_c (a–c), or volume fraction of the gas phase, Φ_b (d–f), for three different alginate concentrations: (a, d) [ALG] = 5% w/w; (b, e) [ALG] = 10% w/w; (c, f) [ALG] = 15% w/w. The dashed lines mark the transition between alternate foam (i.e., two rows of bubbles) and bamboo-like foam (i.e., single row of bubbles).

(entanglement) or physical (e.g., hydrophobic interactions) nature (Figure S1). In the Newtonian range, the viscosity was $\eta_{15\%}$ = 1.1 Pa·s. Values of viscosities as well as the gas–liquid interfacial tensions are reported in Table 1.

A typical foaming experiment consists of setting Q_l and then slowly increasing the gas pressure (P_g). The liquid and gas phases form an interface upstream of the orifice. The pressure drop along the longitudinal axis of the device forces the tip of the gas stream into the orifice. The tip proceeds through the orifice and fills a disk-like gas bubble downstream of the orifice. The growing bubble displaces and pushes away the liquid in the outlet channel. In the orifice, because of the hydrophilic character of the channel walls, the gaseous thread is surrounded by continuous liquid film. Due to the high surface energy of this configuration, the gas thread is not dynamically stable, and it breaks to release a bubble into the outlet channel. To draw calibration diagrams of Φ_b and D_b, it was necessary to scan the pressure range in which bubbles are formed in correspondence with Q_l values between 5 and 60 μL/min.

Because we were interested in fabricating porous materials with percentage porosity >60% v/v as they lead to an interconnected morphology, we concentrated on foams characterized by $\Phi_b \geq 0.4$.

In Figure 2a–c the accessible ranges of bubble diameter (D_b) as a function of P_g and Q_l are displayed. Much important information can be obtained from the analysis of such diagrams. As Q_l increases, the accessible ranges of D_b tend to narrow progressively. For instance, in the case of the solution with the lowest content of alginate (5% w/w), at Q_l = 5 μL/min, bubble diameters span a wide interval, from about 200 to 600 μm, whereas for the highest Q_l = 60 μL/min, they are restricted in the 200–300 μm range (Figure 2a). A similar trend was found also for the other two alginate solutions, 10 and 15% w/w (Figure 2b,c) but with the important difference that for the same values of Q_l, the range of accessible D_b decreases

DOI: 10.1021/acsami.5b08221
ACS Appl. Mater. Interfaces 2015, 7, 23660–23671

significantly as the viscosity of the continuous phase increases. For instance, in the case of 10% w/w alginate solution and Q_l = 40 μL/min, D_b falls in the range of 150−300 μm (Figure 2b), whereas in the case of the 15% w/w alginate solution and the same Q_l, D_b is between 150 and 200 μm (Figure 2c). This behavior is summarized in Figure 3, where bubble volume is

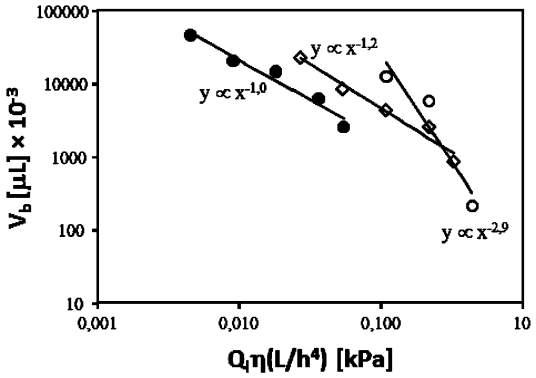

Figure 3. Volume of the bubbles plotted against the product of the flow rate Q_l and viscosity, η, of the liquid phase, scaled to the units of pressure by multiplying by L/h^4. All experiments were performed with p = 10 kPa. Alginate concentrations: (●) 5% w/w; (◇) 10% w/w; (○) 15% w/w.

plotted as a function of the product of viscosity and flow rate of the liquid phase. As can be seen, the experimental points do not fall on a single master curve but follow a power law that is dependent on the viscosity of the liquid phase. This contrasts with previous findings where for a moderate variation of the viscosity, curves collapse on a single master curve.[45] This may be a consequence of the complex fluid properties of the continuous phase used.

In Figure 2d−f, D_b is plotted as a function of Φ_b. From Figure 2d it is evident that for a fixed value of Φ_b, the range of D_b available is relatively narrow in the interval of Q_l explored independently from the continuous phase viscosity. Again, there is a clear influence of solution viscosity on the range of accessible Φ_b. The upper limit reached by Φ_b for the same value of Q_l is progressively shifted downward as η increases. As a consequence, by increasing both parameters η and Q_l it becomes more and more difficult to produce foams characterized by a high values of Φ_b. Another important observation that can be made from Figure 2 is that bubbles arrange into either an alternate (i.e., into two rows) or bamboo-like (i.e., only one row of touching bubbles) fashion, inside the outlet channel. The solid lines drawn in graphs of Figure 2 mark the transition (T_{ab}) from the alternate bubble configuration to a bamboo-like one. As reported in other works, the qualitative foam structure (i.e., arrangements of bubbles in the outlet channel) is a complex function of fluid properties, operating flow parameters, and channel geometry.[46−49] An interesting feature that can be drawn from Figure 2d−f involves the strong dependence of T_{ab} on the viscosity and volumetric flow rate of the liquid phase. This transition is generally expected only at very high values of Φ_b.[50] On the contrary, in our experiments by increasing both parameters η and Q_l, the transition between these two bubble arrangements occurs at lower and lower values of Φ_b. For the most viscous solution, $\eta_{15\%}$, and at the highest flow rate Q_l = 60 μL/min, the transition T_{ab} occurs around Φ_b = 0.4.

The impossibility of preparing foams with a $\Phi_b \geq 0.6$ when using a 10% and, in particular, a 15% w/w alginate solution represents a serious drawback in view of the conversion of such foams into porous solids. It would be desirable to modulate, besides the porous parameters, also scaffold mechanical properties. The stiffness and elasticity of gels have been shown to have a profound effect on cell behavior in 3D cell

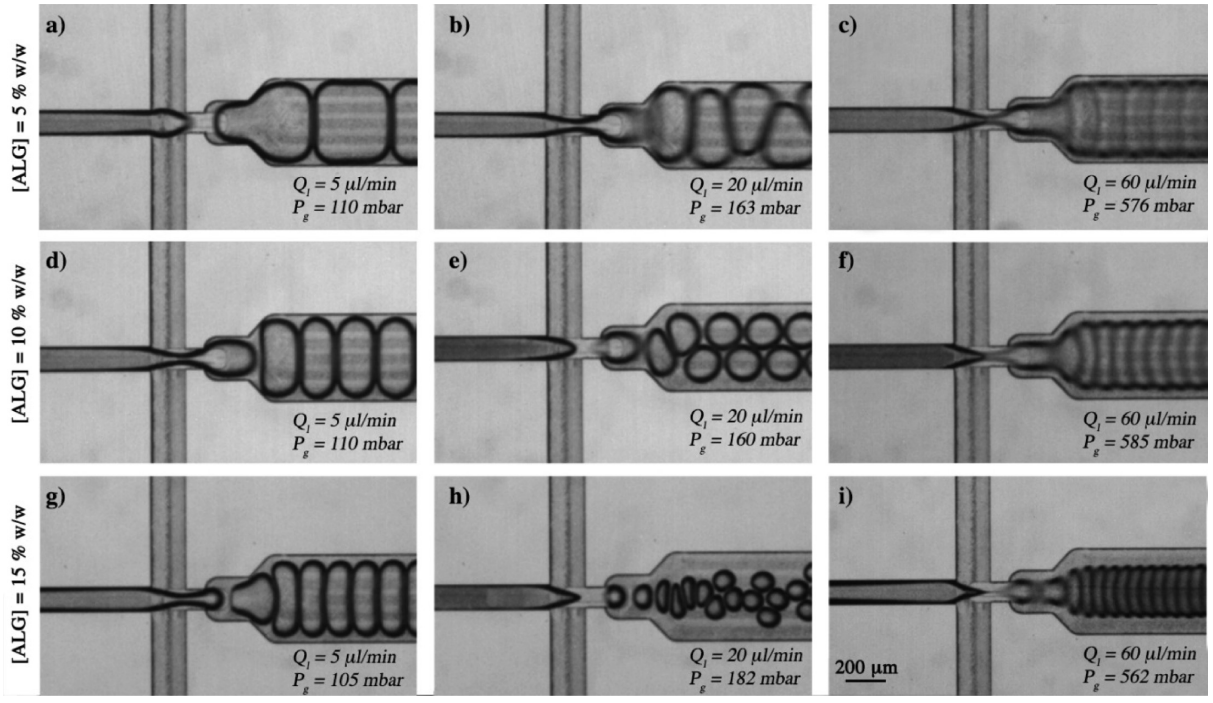

Figure 4. Light micrographs of bubble generation inside the microfluidic chip for three alginate concentrations: (a−c) 5% w/w; (d−f) 10% w/w; (g−i) 15% w/w. The gas pressure and liquid flow rates increase along each row and are approximately constant along each column.

DOI: 10.1021/acsami.5b08221
ACS Appl. Mater. Interfaces 2015, 7, 23660−23671

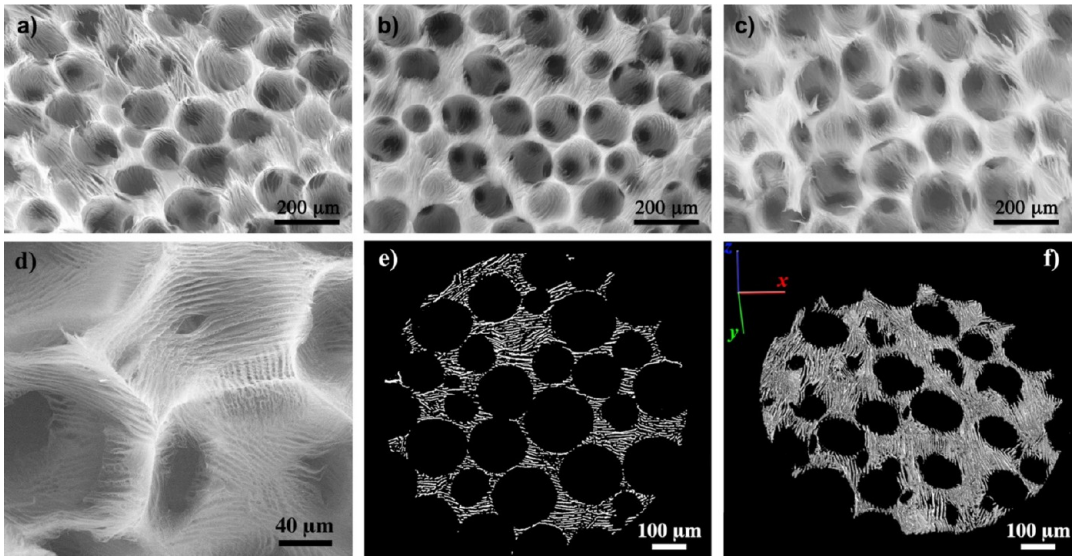

Figure 5. (Top panels) Scanning electron micrographs (SEM) of scaffolds prepared with different volume fractions of the gaseous phase Φ_b and the same pore diameter: (a) 60% v/v; (b) 70% v/v; (c) 80% v/v. (Bottom panels) Details of the microstructure of a scaffold wall as revealed by SEM (d) and high-resolution X-ray microtomography (μCT) (e, f) (voxel size is 1 × 1 × 1 μm). In (e) a random $x-y$ cross section of a scaffold is shown, whereas in (f) a 3D reconstruction 50 μm in thickness is reported.

cultures, and correctly tuning these mechanical properties is critical to the success of the culture.[51] The usual way of tuning the mechanical properties of a scaffold to suit TE applications is to change the concentration of polymer. Thus, understanding the underlying physical phenomena that limit the accessible range of Φ_b in the case of 10 and 15% w/w alginate solutions has practical implications. Examination of the photographs illustrating processes upstream and downstream of the cross-junction of the microfluidic chip (Figure 4) provides some insight. As can be seen the gas finger at the same condition of P_g and Q_l becomes sharper and sharper as the alginate concentration increases. In the same fashion, photographs reported in Figure 4b,e,h illustrate the transition from a bamboo-like to a double-row bubble and to a bubbly flow regime. All of these phenomenological aspects are clearly related to the viscosity of the aqueous phase. A dimensionless variable that provides an estimate of the relative contribution of viscous forces versus surface tension acting across an interface between a liquid and a gas is the capillary number, Ca. The Ca calculated for the flow of the liquid in the orifice is given by $Ca = Q_l\eta/(\sigma w_{or}h)$. The range of Ca values for the three alginate solutions at Q_l = 60 μL/min is reported in Table 1. As expected, the capillary forces, especially for the higher alginate concentrations (10, 15% w/w), can be considered negligible with respect to viscous forces. This range of Ca values suggests the squeezing mechanism of breakup in all of the observed cases. Within this model, as the thread enters the orifice, it restricts the flow of the liquid. The flow of the continuous liquid in the thin films between the gas−liquid interface and the walls of the orifice results in an increased viscous dissipation and a higher pressure drop at the same, fixed value of the liquid flow rate Q_l. The increase of the pressure head over the length of the orifice squeezes the neck connecting the supply of gas with the growing bubble. This squeezing proceeds at a rate proportional to Q_l.[52] We also observe that as the speed of flow increases, the train of bubbles is gradually forced into the central section of the outlet channel. We can explain this observation by the drive of the system to minimize dissipation in the flow of the liquid, by offering it a larger cross section to flow. As a result, we expect the bubbles to flow significantly more quickly than the mean speed of flow. Thus, the observed "apparent" volume fraction of gas, Φ_b, underestimates the volume fraction in the resulting foam.

3.2. Scaffold Characterization. The preliminary results reported in Figure 2 indicate that the most promising candidate for the fabrication of tailored scaffolds is the solution with the lowest alginate content, 5% w/w. Indeed, it is the only solution among the three examined that allows covering the widest range in Φ_b. As a consequence, the first morphological study that was carried out dealt with the control of percentage porosity, P (%). On the basis of results displayed in Figure 2d, we fabricated three different scaffolds with the same pores size (D_b during foam production within the chip was around 260 μm) but different nominal porosities, namely, 60, 70, and 80%. SEM micrographs (Figure 5a−c) illustrate the main morphological features characterizing materials obtained by microfluidic foam templating. In particular, their trabecular and fully interconnected morphology and the qualitative constancy of pore size irrespective of pore volume, P(%), are well evident. Another interesting feature exhibited by all samples is disclosed upon observation at higher magnification of the fine morphology of walls of dry samples. In Figure 5d−f, details of the scaffold walls as revealed by SEM (Figure 5d) and high-resolution μCT analysis (Figure 5e,f) are shown. As can be seen, scaffold walls are characterized by a subporous texture characterized by aligned micropores (no reference is made to IUPAC classification, which defines as micropores those characterized by a dimension ≤2 nm) a few micrometers in size. Such arrays of aligned micropores are originated by the large temperature gradient that orients the ice crystals during the freezing step in liquid nitrogen.[53−55] Solidified water is removed by sublimation, leaving a templated microporous structure where the micropores are a replica of the ice crystals. This microporous texture propagates through the entire wall thickness, generating microducts a few micrometers in size (Figure 5e,f). This fine porosity has a dual effect: the specific

DOI: 10.1021/acsami.5b08221
ACS Appl. Mater. Interfaces 2015, 7, 23660−23671

surface area (SSA) of the scaffolds should be considerably augmented, and the uptake capacity of biological macromolecules (e.g., proteins) from the culture medium should be highly enhanced.[56] Both features could favor cell adhesion on scaffold surfaces and their viability in TE applications.

The 3D renderings obtained from μCT scans of the three scaffolds (Figure 6) illustrate the steady increase of interconnect size as a result of the progressive thinning of the film of continuous film surrounding bubbles. The latter phenomenon is a consequence of the distribution of the liquid phase around an increasing volume of dispersed gas. Image processing of μCT scans, examples of which are reported in Figure S2, allowed estimating accurately pore, interconnect diameter, and wall thickness size distributions for the three scaffolds (Figure 7). The shape of pore size distributions (PSD) (Figure 7a) and the pore diameter ranges covered are remarkably similar in all three cases. PSDs are approximately symmetric with respect to the maximum and span a diameter range from 150 to 250 μm, revealing the invariance of pore size from P (%). As a result, the average pore diameters ($\langle D\rangle$) and the polydispersity indices, $\sigma_{\langle D\rangle}/\langle D\rangle$, as evidenced by data reported in Table 2 (entries 1−3), remain to a large extent constant (≈0.2). Previously, in the case of poly(vinyl alcohol) scaffolds obtained by a conventional foam templating technique, we found a value of polydispersity of 0.45, 225% higher than the present case.[32] Comparison of the diameter of the bubbles D_b produced within the chip (≈260 μm) with the average pore diameter $\langle D\rangle$ (Table 2) indicates that the latter underwent ca. 30% reduction in size during the steps of cross-linking and freeze-drying. The interconnect size distributions (ISD) (Figure 7b) show a progressive skewing toward the high-diameter side as P (%) increases, in accordance with the qualitative observations made from Figure 6. As a result, the values of average interconnect diameters ($\langle d\rangle$) (Table 2, entries 1−3) increase proportionally with P (%). The relative polydispersity indices ($\sigma_{\langle d\rangle}/\langle d\rangle$) are about 33% higher than $\sigma_{\langle D\rangle}/\langle D\rangle$. A reversed trend with respect to ISDs is exhibited by wall thickness distributions (WTDs) (Figure 7c). WTDs are increasingly skewed toward the low size side as P (%) increases, a feature that joined by the trend exhibited by the average pore walls thickness ($\langle$WT$\rangle$; Table 2, entries 1−3) supports the hypothesis of the thinning of the aqueous phase as Φ_b increases.

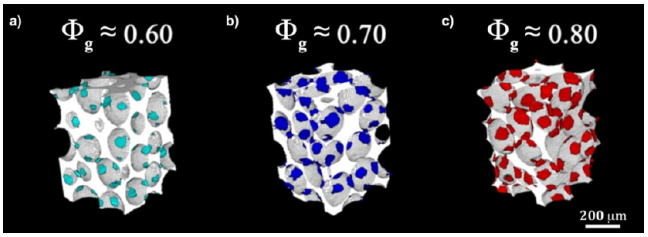

Figure 6. 3D reconstruction of volume of interest (VOI) obtained by μCT scans of three scaffolds prepared with different volume fractions of the gaseous phase Φ_b and the same pore diameter: (a) 60% v/v; (b) 70% v/v; (c) 80% v/v. Areas displayed with colors represent interconnects between adjacent pores.

From μCT image processing, we could determine the average number of interconnects ($\langle N_{int}\rangle_p$) per pore, which is a critical parameter that together with $\langle d\rangle$ affects the permeability properties of the porous materials (Table 2). As can be seen, $\langle N_{int}\rangle_p$ increases steadily as a function of P (%). This result can be explained qualitatively on the basis of Kepler conjecture.[57] When the volume fraction of a monodisperse foam is below 64%, the spherical bubbles are loosely packed and scarcely in contact with each other. This implies that the liquid film separating bubbles will be on average relatively thick, with the consequence that the formation of interconnects in the corresponding materials, which arise from the contact regions between bubbles, is hindered. A dispersed phase volume of 64% represents the upper limit of random packing for monodisperse spheres. Above this percentage, bubbles start being more densely packed and give rise to crystalline regions. The maximum density by an assembly of monodisperse, undeformed bubbles is found at 74% v/v. In this case, bubbles arrange into hexagonal close packed planes (BCC, FCC) characterized by a coordination number of 12 (i.e., each bubble is in contact with another 12 bubbles). This number represents also the theoretical maximum number of interconnects that a pore can have in the final porous matrix. Above 74% v/v, bubbles adopt polyhedral shapes and are separated by a thin film of the liquid phase from which larger interconnects originate. This picture is strictly valid in the case of totally polymerizable continuous phase. In the present case, the scaffold building material represents only 5% w/w of the continuous phase. This probably implies that during the cross-linking and freeze-drying steps, some adjacent interconnects fuse together, determining a $\langle N_{int}\rangle_p$ lower than the theoretical

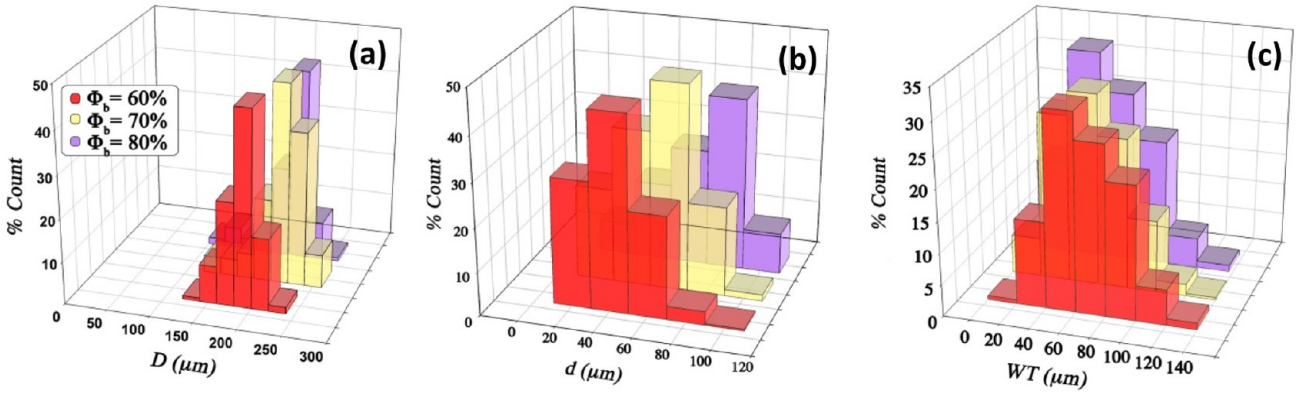

Figure 7. (a) Pore size distributions, (b) interconnect size distributions, and (c) wall thickness distributions of alginate scaffolds characterized by different nominal pore volumes. Alginate concentration in the precursor solution = 5% w/w; surfactant concentration = 5% w/w.

DOI: 10.1021/acsami.5b08221
ACS Appl. Mater. Interfaces 2015, 7, 23660−23671

Table 2. Average Pore Diameters ($\langle D \rangle$) and Normalized Polydispersities ($\sigma_{\langle D \rangle}/\langle D \rangle$), Average Interconnect Diameters ($\langle d \rangle$) and Normalized Polydispersities ($\sigma_{\langle d \rangle}/\langle d \rangle$), Average Wall Thicknesses ($\langle \mathrm{WT} \rangle$) and Normalized Polydispersities ($\sigma_{\langle \mathrm{WT} \rangle}/\langle \mathrm{WT} \rangle$), Porosities ($P$ (%)), Interconnectivities (I (%)), Average Number of Interconnects per Pore ($\langle N_{\mathrm{int}} \rangle_{\mathrm{p}}$), and Permeabilities ($k$) of Alginate Scaffolds Obtained by Employing Different Volume Fractions of the Gas Phase and CTABr Concentrations

	Φ_{b}	[CTABr] (% w/w)	$\langle D \rangle$ (μm)	$\sigma_{\langle D \rangle}/\langle D \rangle$	$\langle d \rangle$ (μm)	$\sigma_{\langle d \rangle}/\langle d \rangle$	$\langle \mathrm{WT} \rangle$ (μm)	$\sigma_{\langle \mathrm{WT} \rangle}/\langle \mathrm{WT} \rangle$	P (%)	I (%)	$\langle N_{\mathrm{int}} \rangle_{\mathrm{p}}$	k (darcy)
1	0.60	5	183	0.19	45	0.33	48	0.41	63	100	6.4	38
2	0.70	5	191	0.22	65	0.28	36	0.53	75	100	7.3	69
3	0.80	5	187	0.21	73	0.28	29	0.51	83	100	8.5	89
4	0.70	1	188	0.21	51	0.34	41	0.41	69	100	6.5	57
5	0.70	0.6	179	0.18	44	0.33	46	0.45	70	100	6.2	41

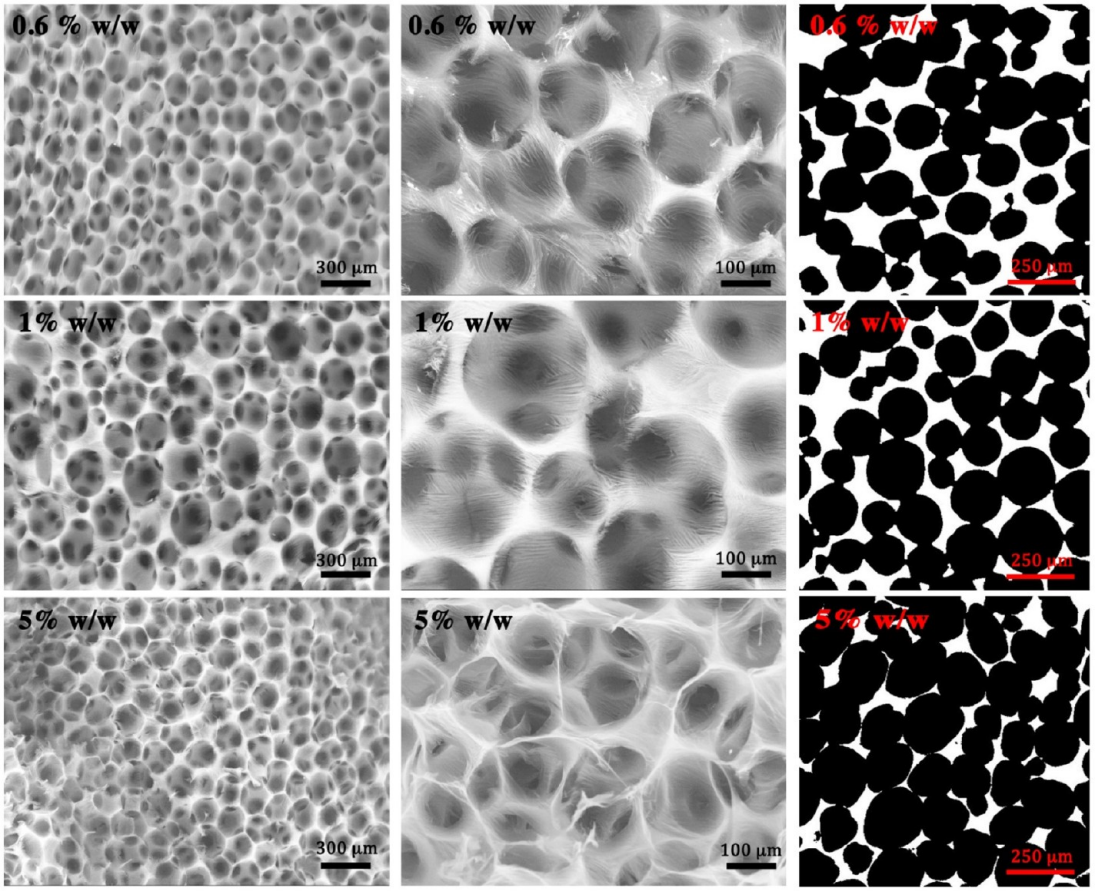

Figure 8. Scanning electron micrographs of alginate solid foams produced by microfluidic foaming taken at various magnifications (left column, 50× magnifications; middle column, 150× magnifications). (Right column) μCT 2D random cross sections of dried samples. From top to bottom, samples prepared with different concentrations of CTABr are shown: 0.6, 1, and 5% w/w.

one. This may also explain the observed discrepancy between $\sigma_{\langle d \rangle}/\langle d \rangle$ and $\sigma_{\langle D \rangle}/\langle D \rangle$ (Table 2, entries 1−3).

An exclusive ability of microfluidics-assisted synthesis of porous materials is the possibility of changing at request one morphological parameter while keeping the others constant. For instance, interconnect size can be varied at request while keeping P (%) and $\langle D \rangle$ constant. This morphological feature is probably the most important one in applications such as tissue engineering because it determines cellular infiltration, proliferation, and spreading. Moreover, cell viability is favored only if the supply of nutrients and oxygen and the disposal of metabolic wastes are efficient throughout the scaffold. In flow-through applications, the resistance to fluid flow will be maintained low only if a good degree of interconnectivity is guaranteed throughout the matrix. The size of interconnects is strictly related to the thickness of the aqueous film surrounding bubbles in the precursor foam. The size and thickness of this film in a foam are controlled by the pressure difference between the continuous and the dispersed phase (i.e., the capillary pressure). This pressure difference increases with decreasing interfacial tension and with increasing volume fraction of the dispersed phase. We have seen (Table 2, entries 1−3) that changing Φ_{b} affects both $\langle D \rangle$ and $\langle d \rangle$. It could be of practical interest to decouple the variation of $\langle d \rangle$ from that of $\langle D \rangle$. This can be achieved through the variation of surfactant concentration. To illustrate this approach, we prepared another two samples with the same pore sizes (D_{b}, during foam production within the chip, was always around 260 μm) and the same Φ_{b} = 0.7. The only compositional parameter in which they differ is the concentration of surfactant, [CTABr], in the precursor alginate solution. The series of alginate solutions characterized by a different [CTABr] is thus 0.6, 1.0, and 5% w/w. In Figure

DOI: 10.1021/acsami.5b08221
ACS Appl. Mater. Interfaces 2015, 7, 23660−23671

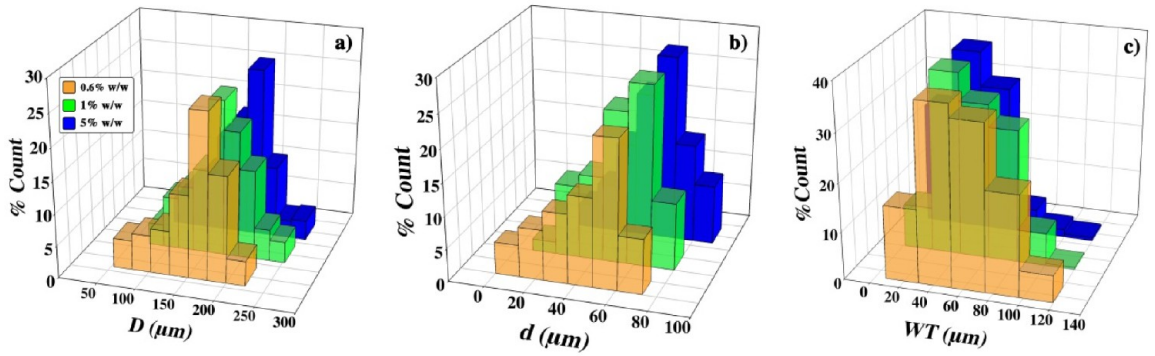

Figure 9. (a) Pore size distribution, (b) interconnect size distribution, and (c) wall thickness distribution of scaffolds prepared with different concentrations of CTABr. [CTABr]: (a) 0.6% w/w; (b) 1% w/w; (c) 5% w/w.

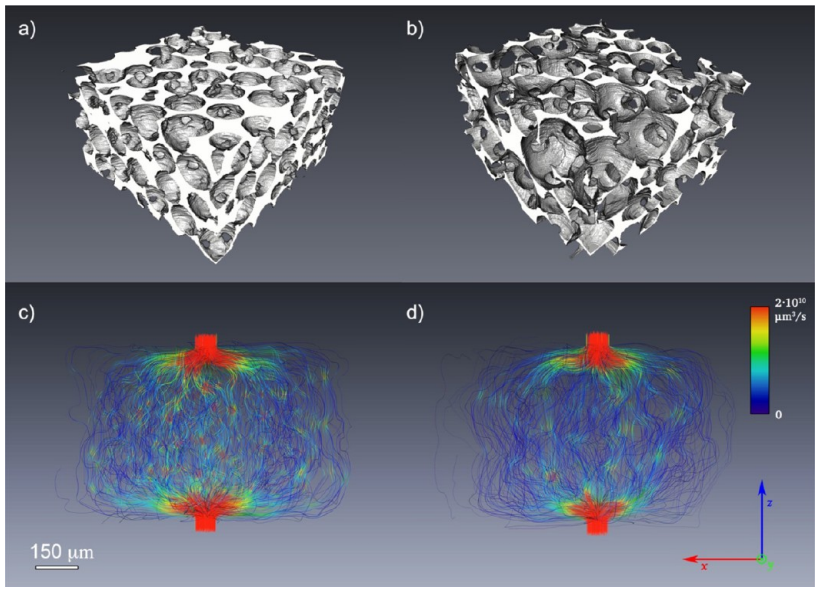

Figure 10. 3D rendering of two different porous matrices characterized by different pore volumes ((a) 63%, (b) 83%) and representation of the streamlines flowing through the scaffold pores and interconnects (c, d). The calibrated color bar permits the correlation between colors and local velocities.

8(left and middle columns) SEM micrographs taken at different magnifications and 2D μCT cross sections (Figure 8, right column) of the three scaffolds evidence clearly the widening of interconnects as the concentration of surfactant increases. In Figure 9a, the corresponding PSDs and $\langle D \rangle$ (Table 2, entries 2, 4, and 5) confirm the invariance of pore size from surfactant concentration. On the contrary, ISDs (Figure 9b) shift progressively toward the high diameter side as [CTABr] increases. As a result, $\langle d \rangle$ values undergo a concomitant increase in size of about 48% (Table 2, entries 2, 4, and 5). In Figure S3 the colored distance maps of WT and the relative 3D renderings obtained from μCT scans illustrate the decrease of wall thickness as a function of the surfactant concentration. As expected, WSDs reported in Figure 9c follow the reverse trend with respect ISDs. The observed reduction in $\langle$WT$\rangle$ (Table 2, entries 2, 4, and 5) was around 22%.

The origin of the observed trends for ISDs and WSDs is that the increase of surfactant concentration brings about a lowering of the water/gas interfacial tension. Measured values of interfacial tension for [CTABr] equal to 0.6, 1.0, and 5% w/w were 51.3, 48.6, and 35.6 mN/mm, respectively. When adjacent bubbles touch one each other, their propensity to flatten, forming facets from which the interconnects later originate, is enhanced as [CTABr] increases. These facets can be interpreted as thin films of surfactant molecules that prevent the neighboring bubbles from coalescing. We speculate that by lowering surface tension, bubbles become more adhesive and, in turn, regions of adhesion widen, thus generating larger interconnects.

Finally, we used the data obtained by means of μCT scans to carry out computational fluid dynamic (CFD) simulations of permeability through the porous matrices. Permeability is defined as the measure of the ability of a porous material to transmit a single-phase fluid. It appears in Darcy's law as a constant coefficient relating fluid, flow, and material parameters:

$$\frac{Q}{S} = -\frac{k}{\mu}\frac{\Delta P}{L}$$

Q is the flow rate of the fluid that flows through the porous material, S is the area of the cross section of the sample, k is the permeability, μ is the dynamic viscosity of the flowing fluid, and $\Delta P/L$ is the pressure drop per unit of length of the porous medium.

DOI: 10.1021/acsami.5b08221
ACS Appl. Mater. Interfaces 2015, 7, 23660−23671

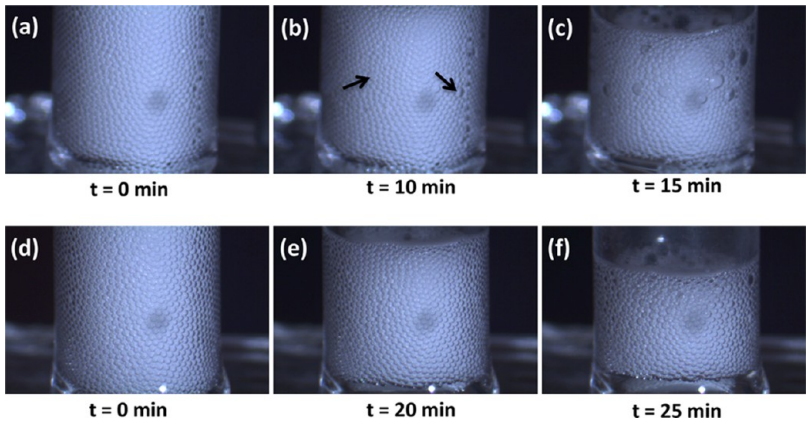

Figure 11. Time evolution of two monodisperse foams characterized by two different surfactant concentrations: (a–c) 0.6% w/w; (d–f) 5% w/v. The alginate concentration is 5% w/w. Arrows in (b) indicate the onset of first coalescence phenomena within the foam.

In Figure 10c,d the representation of the flow streamlines along one direction is shown in the case of two matrices (Table 2, entries 1 and 3) characterized by very different interconnect sizes and for which 3D renderings are shown in Figure 10a,b. An example of animation of streamlines flowing through pores and interconnects is reported in the Supporting Information. As can be seen (Figure 10c,d), streamlines follow a regular path with sinusoidal-like profiles. In the proximity of interconnects they converge and then expand inside the pores. As can be appreciated through the calibrated bar correlating colors and local velocities, fluid velocity in the expansion decelerates from a high velocity in the contraction. Moreover, it appears clearly that streamlines are well distributed within the analyzed volume, implying that the number of preferential paths is very limited. This is a very crucial feature for tissue engineering application of these materials and more specifically for application within perfusion systems for cell seeding and culture. As can be seen (Figure 10c) in the matrix with smaller interconnects, zones of higher local velocities are found in correspondence to interconnects as evidenced by bundles of red streamlines. Data referring to the permeabilities of all the scaffolds produced are reported in Table 2. As expected, the results show that there is a strict correlation between permeabilities, the average interconnect diameter $\langle d \rangle$, and the average number of interconnects per pore $\langle N_{int} \rangle_p$. The most permeable scaffold turned out to be the sample characterized by the largest porosity, the largest $\langle d \rangle$, and the highest value of $\langle N_{int} \rangle_p$.

We acknowledge that the permeability value obtained through CFD simulations within 1 mm^3 VOI must be interpreted carefully and may differ from the real value. A potential bias in the determination of permeability of scaffolds may arise from the fact that CFD simulations were performed on μCT reconstructed structures of lyophilized matrices. The microarchitecture of the matrices could significantly differ between dry and hydrated conditions as a consequence of some degree of swelling of the matrices. Nevertheless, simulations are useful because they permit to put into evidence the correlation between the scaffolds' morphological features and their relative permeability.

3.3. Foam Production Rate. A major concern when exploiting microfluidic foaming as a scaffold fabrication technique is represented by the limited temporal stability of gas-in-liquid foams in conjunction with the limited production rate. Despite monodisperse foams enjoying a longer life span than polydispersed ones, because Ostalwald ripening (i.e., the increase of larger droplets at the expense of smaller ones) in the former is inhibited, they are subject to liquid drainage. This phenomenon is driven by the large difference in density between the liquid and gas phases and causes the progressive thinning and thickening of the liquid film in the upper and lower portions of the foam, respectively. Thus, the advantages offered by microfluidic foaming in terms of uniformity in porous textures tend to be lost if the foam collecting step is protracted beyond a certain temporal limit. As a consequence, it is fundamental to establish the temporal window within which foams can be collected without destabilization phenomena taking place to any significant extent. To this end we have collected in a very short time (≈30 s) a small amount of two foams (5% w/w alginate; 0.6 and 5% w/w CTABr) in a glass vial (characterized by the same height/diameter ratio as the ones used in previous studies) and let them stand. Photographs were recorded every minute, and representative pictures are reported in Figure 11. As can be seen (Figure 11a), the 0.6% w/w CTABr foam was stable for a period of time ≤10 min. This time limit marks the occurrence of the first sign of coarsening. For times >10 min, coarsening of the foam accelerates and gas escapes from the foam as witnessed by the lowering of the foam level. In the case of 5% w/w CTABr foam, destabilization is manifested by drainage, the bubbles' dimension remaining approximately constant during this process (Figure 11b). This phenomenon starts being observable for time >15 min. Because for Q_l = 60 μL/min and P_g = 250 mbar the foam production rate is 0.3 mL/min, the volumes that can be safely collected are 3, 4, and 5 mL for the 0, 6, and 5% w/w CTABr solutions, respectively. These amounts are adequate for characterization studies but insufficient for many practical purposes. The only viable way to increase substantially foam production is by chip parallelization analogously to what has been done with microfluidics microparticle production.[58] This issue is currently the subject of intensive research, and devices opportunely designed have been proposed. For instance, Kendall et al.[59] have developed a multiarray microfluidic module capable of generating large amounts of multilayer microbubbles, with good monodispersity.

Despite the present shortcomings, microfluidics-assisted synthesis of scaffolds holds strong promise in the field of tissue engineering. It has been demonstrated that the uniformity in pore size and structure of microfluidic scaffolds

DOI: 10.1021/acsami.5b08221
ACS Appl. Mater. Interfaces 2015, 7, 23660–23671

leads to a higher diffusion rate and a more uniform distribution of cells than its counterpart with nonuniform pores.[34]

4. CONCLUSION

In this work we have shown that a microfluidic foaming technique is a versatile and powerful tool to generate scaffolds with tailored morphological and permeability properties.

This technique allows independent control of pore size, percentage porosity, and, to some extent, interconnect size. The experimental parameters that control these features are the bubble volume, the interfacial tension between the two phases, and the volume fraction of the gaseous phase in the precursor foam. The ranges in which these parameters can be tuned are generally broad. However, the determination of calibration diagrams for the particular microfluidic chip used are always needed to foresee the available ranges for D_b and Φ_b. We demonstrated that the viscosity of the liquid phase, especially at high values of the flow rate, adversely affect the accessible ranges of Φ_b. Therefore, we were forced to use the alginate solution with relatively low viscosity because it allowed a higher degree of flexibility in the creation of solid foams with tunable porous characteristics and with the highest production rate. Thus, as a general rule, we can postulate that it is always better to process low viscous, Newtonian-like solutions because they allow wider ranges of D_b and Φ_b to be covered and, at the same time, the foam production rate is higher when compared with more viscous solutions. Moreover, we demonstrated by means of CFD simulations that interconnect size and the average number of interconnects per pore greatly influence the permeability of the scaffolds, thus further emphasizing the importance of controlling their size. A factor that limits the extensive use of microfluidic foaming as a scaffold fabrication technique is the scarce volume throughput per unit time in conjunction with the limited foam life span. The design of microfluidics reactors containing multiple chips working in parallel is the only viable route to speed foam production and exploit the potentials of microfluidic foaming in the manufacturing of scaffolds for tissue engineering.

The scaffolds presented in this work are currently being tested in bone marrow-derived human mesenchymal stromal cells (hBMSC) seeding and culture experiments under perfusion conditions. To highlight their superior performance in terms of biological response, microfluidics scaffolds are being compared with scaffolds obtained by conventional gas foaming.[32,33,41] Results of these studies will be the subject of a forthcoming publication.

■ ASSOCIATED CONTENT

Supporting Information

The Supporting Information is available free of charge on the ACS Publications website at DOI: 10.1021/acsami.5b08221.

Video of simulations of the fluid flow through the scaffolds (AVI)

Viscosity versus shear rate for different alginate concentration solutions; 3D representation of the main morphological features of the porous scaffolds; colored distance maps of scaffold wall thickness (PDF)

■ AUTHOR INFORMATION

Corresponding Author

*(A.B.) E-mail: andrea.barbetta@uniroma1.it.

Notes

The authors declare no competing financial interest.

■ ACKNOWLEDGMENTS

We thank Sapienza University of Rome for funding this research (Ateneo Funds). P.G. acknowledges funding within the European Research Council Starting Grant 279647.

■ REFERENCES

(1) Al-Abboodi, A.; Fu, J.; Doran, P. M.; Tan, T. T. Y.; Chan, P. P. Y. Injectable 3D Hydrogel Scaffold with Tailorable Porosity Post-Implantation. *Adv. Healthcare Mater.* **2014**, *3*, 725−736.

(2) Ren, K.; He, C.; Cheng, Y.; Li, G.; Chen, X. Injectable Enzymatically Crosslinked Hydrogels Based on a Poly(L-glutamic acid) Graft Copolymer. *Polym. Chem.* **2014**, *5*, 5069−5076.

(3) Assaad, E.; Maire, M.; Lerouge, S. Injectable Thermosensitive Chitosan Hydrogels with Controlled Gelation Kinetics and Enhanced Mechanical Resistance. *Carbohydr. Polym.* **2015**, *130*, 87−96.

(4) Ahmadi, R.; Mordan, N.; Forbes, A.; Day, R. Enhanced Attachment, Growth and Migration of Smooth Muscle Cells on Microcarriers Produced Using Thermally Induced Phase Separation. *Acta Biomater.* **2011**, *7*, 1542−1549.

(5) Barroca, N.; Daniel-da-Silva, S.; Vilarinho, P.; Fernandes, M. Tailoring the Morphology of High Molecular Weight PLLA Scaffolds Through Bioglass Addition. *Acta Biomater.* **2010**, *6*, 3611−3620.

(6) He, L.; Zhang, Y.; Zeng, X.; Quan, D.; Liao, S.; Zeng, Y.; Lu, J.; Ramakrishna, S. Fabrication and Characterization of Poly(L-lactic acid) 3D Nanofibrous Scaffolds with Controlled Architecture by Liquid-Liquid Phase Separation from a Ternary Polymer-Solvent System. *Polymer* **2009**, *50*, 4128−4138.

(7) Mooney, D. J.; Baldwin, D. F.; Suh, N. P.; Vacanti, J. P.; Langer, R. Novel Approach to Fabricate Porous Sponges of PolyD,L-lactic-*co*-glycolic acid) Without the Use of Organic Solvents. *Biomaterials* **1996**, *17*, 1417−1422.

(8) Lu, L.; Peter, S. J.; Lyman, M. D.; Lai, H.-L.; Leite, S. M.; Tamada, J. A.; Uyama, S.; Vacanti, J. P.; Langer, R.; Mikos, A. G. In Vitro and in Vivo Degradation of Porous Poly(D,L-lactic-*co*-glycolic acid) Foams. *Biomaterials* **2000**, *21*, 1837−1845.

(9) Zhang, J.; Wu, L.; Jing, D.; Ding, J. A Comparative Study of Porous Scaffolds with Cubic and Spherical Macropores. *Polymer* **2005**, *46*, 4979−4985.

(10) Park, J. S.; Woo, D. G.; Sun, B. K.; Chung, H.-M.; Im, S. J.; Choi, Y. M.; Park, K.; Huh, K. M.; Park, K.-H. In Vitro and in Vivo Test of Polyethylene Glycol/Poly *ε*-caprolactone Based Hydrogel Scaffold for Cell Delivery Application. *J. Controlled Release* **2007**, *124*, 51−59.

(11) Barbetta, A.; Gumiero, A.; Pecci, R.; Bedini, R.; Dentini, M. Gas-in-Liquid Foam Templating as a Method for the Production of Highly Porous Scaffolds. *Biomacromolecules* **2009**, *10*, 3188−3192.

(12) Lips, P. A. M.; Velthoen, I. W.; Dijkstra, P. J.; Wessling, M.; Feijen, J. Gas Foaming of Segmented Poly(ester amide) Films. *Polymer* **2005**, *46*, 9396−9403.

(13) Caykara, T.; Kucuktepe, S.; Turan, E. Swelling Characteristics of Thermo-Sensitive Poly[(2-diethylaminoethyl methacrylate)-*co*-(*N*,*N*-dimethylacrylamide)] Porous Hydrogels. *Polym. Int.* **2007**, *56*, 532−537.

(14) Huh, K. M.; Baek, N.; Park, K. Enhanced Swelling Rate of Poly(ethylene glycol)-Grafted Superporous Hydrogels. *J. Bioact. Compat. Polym.* **2005**, *20*, 231−243.

(15) Keskar, V.; Marion, N. W.; Mao, J. J.; Gemeinhart, R. A. In Vitro Evaluation of Macroporous Hydrogels to Fabricate Stem Cell Infiltration, Growth, and Mineralization. *Tissue Eng., Part A* **2009**, *15*, 1695−1707.

(16) Barbetta, A.; Dentini, M.; De Vecchis, M. S.; Filippini, P.; Formisano, G.; Caiazza, S. Scaffolds Based on Biopolymeric Foams. *Adv. Funct. Mater.* **2005**, *15*, 118−124.

(17) De Colli, M.; Massimi, M.; Barbetta, A.; Di Rosario, B.; Nardecchia, S.; Conti Devirgiliis, L.; Dentini, M. A Biomimetic Porous

DOI: 10.1021/acsami.5b08221
ACS Appl. Mater. Interfaces 2015, 7, 23660−23671

Hydrogel Made of Gelatin and Glycosaminoglycans Tested for Hepatocyte Cultures. *Biomed. Mater.* **2012**, *7*, 055005.
(18) Oh, B. H. L.; Bismarck, A.; Chan-Park, M. B. Injectable, Interconnected, High-Porosity Macroporous Biocompatible Gelatin Scaffolds Made by Surfactant-Free Emulsion Templating. *Macromol. Rapid Commun.* **2015**, *36*, 364−372.
(19) Barbetta, A.; Massimi, M.; Conti Devirgiliis, L.; Dentini, M. Enzymatic Cross-Linking versus Radical Polymerization in the Preparation of Gelatin PolyHIPEs and Their Performance as Scaffolds in the Culture of Hepatocytes. *Biomacromolecules* **2006**, *7*, 3059−3068.
(20) Thomson, R. C.; Wake, M. C.; Yaszemski, M. J.; Mikos, A. G. Biodegradable Polymer Scaffolds to Regenerate Organs. *Adv. Polym. Sci.* **1995**, *122*, 245−274.
(21) Wu, X.; Black, L.; Santacana-Laffitte, G.; Patrick, C. W., Jr. Preparation and Assessment of Glutaraldehyde-Crosslinked Collagen-Chitosan Hydrogels for Adipose Tissue Engineering. *J. Biomed. Mater. Res., Part A* **2007**, *81*, 59−65.
(22) Jin, R.; Moreira Teixeira, L. S.; Dijkstra, P. J.; Karperien, M.; Zhong, Z.; Feijen, J. Fast in-Situ Formation of Dextrantyramine Hydrogels for in Vitro Chondrocyte Culturing. *J. Controlled Release* **2008**, *132*, e24−e26.
(23) Lv, Q.; Hu, K.; Feng, Q.; Cui, F. Fibroin/Collagen Hybrid Hydrogels with Crosslinking Method: Preparation, Properties, and Cytocompatibility. *J. Biomed. Mater. Res., Part A* **2008**, *84*, 198−207.
(24) Kang, H. W.; Tabata, Y.; Ikada, Y. Fabrication of Porous Gelatin Scaffolds for Tissue Engineering. *Biomaterials* **1999**, *20*, 1339−44.
(25) Mikos, A. G.; Lu, L.; Temenoff, J. S.; Tessmar, J. K. In *Biomaterials Science*; Ratner, B. D., Hoffman, A. S., Schoen, F. J., Lemons, J. E., Eds.; Elsevier: San Diego, CA, USA, 2004; pp 735−749.
(26) Dai, W.; Kawazoe, N.; Lin, X.; Dong, J.; Chen, G. The Influence of Structural Design of PLGA/Collagen Hybrid Scaffolds in Cartilage Tissue Engineering. *Biomaterials* **2010**, *31*, 2141−2152.
(27) Annabi, N.; Nichol, J. W.; Zhong, X.; Ji, C.; Koshy, S.; Khademhosseini, A.; Dehghani, F. Controlling the Porosity and Microarchitecture of Hydrogels for Tissue Engineering. *Tissue Eng., Part B* **2010**, *16*, 371−383.
(28) Dehghani, F.; Annabi, N. Engineering Porous Scaffolds Using Gas-Based Techniques. *Curr. Opin. Biotechnol.* **2011**, *22*, 661−666.
(29) Puppi, D.; Chiellini, F.; Piras, A. M.; Chiellini, E. Polymeric Materials for Bone and Cartilage Repair. *Prog. Polym. Sci.* **2010**, *35*, 403−440.
(30) Linnes, M. P.; Ratner, B. D.; Giachelli, C. M. A fibrinogen-Based Precision Microporous Scaffold for Tissue Engineering. *Biomaterials* **2007**, *28*, 5298−5306.
(31) Liu, X.; Smith, L. A.; Hu, J.; Ma, P. X. Biomimetic Nanofibrous Gelatin/Apatite Composite Scaffolds for Bone Tissue Engineering. *Biomaterials* **2009**, *30*, 2252−2258.
(32) Colosi, C.; Costantini, M.; Barbetta, A.; Pecci, R.; Bedini, R.; Dentini, M. Morphological Comparison of PVA Scaffolds Obtained by Gas Foaming and Microfluidic Foaming Techniques. *Langmuir* **2013**, *29*, 82−91.
(33) Costantini, M.; Colosi, C.; Guzowski, J.; Barbetta, A.; Jaroszewicz, J.; Święszkowski, W.; Dentini, M.; Garstecki, P. Highly Ordered and Tunable PolyHIPEs by Using Microfluidics. *J. Mater. Chem. B* **2014**, *2*, 2290−2300.
(34) Lin, J.; Lin, W.; Hong, W.; Hung, W.; Nowotarski, S. H.; Montenegro Gouveia, S.; Cristo, I.; Lin, K. Morphology and Organization of Tissue Cells in 3D Microenvironment of Monodisperse Foam Scaffolds. *Soft Matter* **2011**, *7*, 10010−10016.
(35) Sun, Y.-S.; Peng, S.-W.; Lin, K.-H.; Cheng, J.-Y. Electrotaxis of Lung Cancer Cells in Ordered Three-Dimensional Scaffolds. *Biomicrofluidics* **2012**, *6*, 014102.
(36) Lee, Y.; Huang, J.; Wang, Y.; Lin, K. Three-Dimensional Fibroblast Morphology on Compliant Substrates of Controlled Negative Curvature. *Integr. Biol.* **2013**, *5*, 1447−1455.
(37) Hunt, N.; Grover, C. L. M. Cell Encapsulation Using Biopolymer Gels for Regenerative Medicine. *Biotechnol. Lett.* **2010**, *32*, 733−742.
(38) Spiller, K. L.; Maher, S. A.; Lowman, A. M. Hydrogels for the Repair of Articular Cartilage Defects. *Tissue Eng., Part B* **2011**, *17*, 281−89.
(39) Seliktar, D. Designing Cell-Compatible Hydrogels for Biomedical Applications. *Science* **2012**, *336*, 1124−28.
(40) Zhou, S.; Bismarck, A.; Steinke, J. H. G. Ion-Responsive Alginate Based Macroporous Injectable Hydrogel Scaffolds Prepared by Emulsion Templating. *J. Mater. Chem. B* **2013**, *1*, 4736−4745.
(41) Barbetta, A.; Barigelli, E.; Dentini, M. Porous Alginate Hydrogels: Synthetic Methods for Tailoring the Porous Texture. *Biomacromolecules* **2009**, *10*, 2328−2337.
(42) Martynov, S.; Wang, X.; Stride, E. P.; Edirisinghe, M. J. Preparation of a Micro-Porous Alginate Gel Using a Microfluidic Bubbling Device. *Int. J. Food Eng.* **2010**, *6*, No. 8, DOI: 10.2202/1556-3758.1774.
(43) Raven, J. P.; Marmottant, P.; Graner, F. Dry Microfoams: Formation and Flow in a Confined Channel. *Eur. Phys. J. B* **2006**, *51*, 137−143.
(44) Marmottant, P.; Raven, J.-P. Microfluidics with Foams. *Soft Matter* **2009**, *5*, 3385−3388.
(45) Garstecki, P.; Gitlin, I.; DiLuzio, W.; Whitesides, G. M.; Kumacheva, E.; Stone, H. A. Formation of Monodisperse Bubbles in a Microfluidic Flow-Focusing Device. *Appl. Phys. Lett.* **2004**, *85*, 2649−2651.
(46) Park, J. I.; Tomarkin, E.; Kumacheva, E. Small, Stable, and Monodispersed Bubbles Encapsulated with Biopolymers. *Macromol. Rapid Commun.* **2010**, *31*, 222−227.
(47) Raven, J. P.; Marmottant, P.; Graner, F. Dry Microfoams: Formation and Flow in a Confined Channel. *Eur. Phys. J. B* **2006**, *51*, 137−143.
(48) Gañán-Calvo, A. M.; Gordillo, J. M. Perfectly Monodisperse Microbubbling by Capillary Flow Focusing. *Phys. Rev. Lett.* **2001**, *87*, 274501.
(49) Vuong, S. M.; Anna, S. L. Tuning Bubbly Structures in Microchannels. *Biomicrofluidics* **2012**, *6*, 022004−18.
(50) Huerre, A.; Miralles, V.; Jullien, M. Bubbles and Foams in Microfluidics. *Soft Matter* **2014**, *10*, 6888−6902.
(51) Dessi, M.; Borzacchiello, A.; Mohamed, T. H. A.; Abdel-Fattah, W. I.; Ambrosio, L. Novel Biomimetic Thermosensitive β-Tricalcium Phosphate/Chitosan-Based Hydrogels for Bone Tissue Engineering. *J. Biomed. Mater. Res., Part A* **2013**, *101A*, 2984−2993.
(52) Garstecki, P.; Stone, H. A.; Whitesides, G. M. Mechanism for Flow-Rate Controlled Breakup in Confined Geometries: A Route to Monodisperse Emulsions. *Phys. Rev. Lett.* **2005**, *94*, 164501.
(53) Gutierrez, M. C.; Ferrer, M. L.; Del Monte, F. Ice Templated Materials: Sophisticated Structures Exhibiting Enhanced Functionalities Obtained after Unidirectional Freezing and Ice Segregation Induced Self-Assembly. *Chem. Mater.* **2008**, *20*, 634−648.
(54) Deville, S. Freeze-Casting of Porous Ceramics: A Review of Current Achievements and Issues. *Adv. Eng. Mater.* **2008**, *10*, 155−169.
(55) Zhang, H.; Hussain, I.; Brust, M.; Butler, M. F.; Rannard, S. P.; Cooper, A. I. Aligned two- and Three-Dimensional Structures by Directional Freezing of Polymers and Nanoparticles. *Nat. Mater.* **2005**, *4*, 787−793.
(56) Woo, K. M.; Chen, V. J.; Ma, X. P. Nano-Fibrous Scaffolding Architecture Selectively Enhances Protein Adsorption Contributing to Cell Attachment. *J. Biomed. Mater. Res.* **2003**, *67A*, 531−537.
(57) Aste, T.; Weaire, D. *The Pursuit of Perfect Packing*; Institute of Physics Publishing: London, UK, 2000.
(58) Nisisako, T.; Torii, T. Microfluidic Large-Scale Integration on a Chip for Mass Production of Monodisperse Droplets and Particles. *Lab Chip* **2008**, *8*, 287−293.
(59) Kendall, M. R.; Bardin, D.; Shih, R.; Dayton, P. A.; Lee, A. P. Scaled-up Production of Monodisperse, Dual Layer Microbubbles Using Multi-Array Microfluidic Module for Medical Imaging and Drug Delivery. *Bubble Sci., Eng., Technol.* **2012**, *4*, 12−20.

DOI: 10.1021/acsami.5b08221
ACS Appl. Mater. Interfaces 2015, 7, 23660−23671